



Artificial Neural Network (ANN)-Based Residual Strength Prediction of Carbon Fibre Reinforced Composites (CFRCs) After Impact

Bin Yang¹ · Kunkun Fu^{1,2} · Juhyeong Lee³ · Yan Li¹

Received: 14 September 2020 / Accepted: 15 March 2021 / Published online: 12 April 2021
© The Author(s), under exclusive licence to Springer Nature B.V. 2021

Abstract

This study presents an artificial neural network (ANN) model for predicting the residual strength of carbon fibre reinforced composites (CFRCs) after low-velocity impact. First, a finite element (FE) model was developed addressing intra-laminar damage and inter-laminar delamination, to estimate low-velocity impact (LVI) and compression-after-impact (CAI) responses of CFRCs. The FE results in terms of load–displacement curves, damage patterns, and residual strengths were found to be essentially in agreement with those by experiments. An ANN model was developed using back-propagation learning algorithm and was trained using the FE results to establish a nonlinear relationship between LVI parameters (i.e. impact energy and impactor diameter) and CFRC residual strength. Twelve sets of additional CAI simulations were carried out to validate the proposed ANN-based residual strength prediction model. A good agreement was achieved between the residual strengths predicted by ANN model and the FE results with errors less than 5%, demonstrating the effectiveness of the present ANN model. The established ANN-based model can effectively reduce the experimental costs and computational time.

Keywords Artificial neural network (ANN) · Residual strength · Carbon fibre reinforced composites (CFRCs) · Compression-after-impact (CAI)

✉ Kunkun Fu
1984fukunkun@tongji.edu.cn

Juhyeong Lee
juhyeong.lee@usu.edu

¹ School of Aerospace Engineering and Applied Mechanics, Tongji University, Shanghai 200092, P.R. China

² State Key Laboratory for Strength and Vibration of Mechanical Structures, Xi'an Jiaotong University, Xi'an 710049, P.R. China

³ Department of Mechanical and Aerospace Engineering, Utah State University, Logan, UT 84322-4130, USA

1 Introduction

Carbon fibre reinforced composites (CFRCs) have been increasingly used in aerospace, automotive, and wind turbine applications. In comparison to traditional metallic materials, CFRCs have many advantages such as excellent specific strength and stiffness, high resistance to corrosion and fatigue [1–3]. However, CFRCs are vulnerable to foreign object impacts (i.e. tool drops, bird strike, hail/ice impact) due to their intrinsically brittle failure nature [4, 5]. The damage introduced by an accidental impact may substantially reduce the structural stiffness and integrity, leading to a significant drop in residual strength. Compression-after-impact (CAI) strength, which attracted increasingly attentions to both academia and industry, is a well-known material property to assess the structural integrity of CFRCs after impact.

Over the decades, low-velocity impact (LVI) response and failure analysis of CFRCs have been extensively investigated [6–10]. The damages such as fibre fracture, matrix cracking, and delamination caused by LVI depend on the level of the applied impact energy. These can reduce the residual mechanical properties of CFRCs [11–15]. The failure process of CFRCs with LVI damage is difficult to predict when combined with in-plane compression. The LVI-induced damage in CFRC may trigger local stress concentration, resulting in fibre fracture, matrix cracking or delamination, and eventually structural collapse [16–18].

Various experimental and numerical methods have been presented for predicting the CAI strength of laminates in recent years. The CAI strength of CFRCs with LVI-induced damage are closely related to laminate type, ply thickness, stacking sequence, impactor shape, and impact energy. Liu et al. [19, 20] conducted a series of LVI and CAI tests to understand the failure mechanism of hybrid unidirectional (UD) and plain woven fabric (WF) CFRCs subjected to in-plane compression. The outermost WF plies improved the composite CAI strength since the woven plies could constrain the extent of damage during impact. Cheng and Xiong [9] demonstrated that the laminate type has an evident effect on LVI and CAI behaviour of composite materials, and the CAI strength of CFRCs was nearly 1.5 times higher than that of glass fibre reinforced composites. Caminero et al. [21] examined the effect of stacking sequence on the CAI strength of CFRCs and they found that cross-ply laminates exhibited lower CAI strengths than angle-ply laminates. The low CAI strength of the CFRCs may be due to the fact that the 90° plies made the central sub-laminate less stiff, more unstable, and liable to fail subjected to a smaller load. González et al. [22, 23] developed a 3D finite element (FE) model predicting inter-laminar and intra-laminar damage to evaluate the LVI and CAI behaviours of CFRC, and they found that the laminate CAI strength is fairly sensitive to the stacking sequence. Habibi et al. [24] performed experimental and numerical studies to characterize the influence of impactor shape and impact energy on the LVI and CAI behaviours of CFRCs. In general, the CAI strength decreased with the increase of impact energy and number of multiple impacts [25].

It is well known that the experiments on the CAI strength of CFRC with LVI damage often require a lot of manpower, materials, and financial resources. For instance, to meet the damage tolerance airworthiness requirement, composite structures in aircraft with many types of damage (i.e., barely visible impact damage, visible impact damage, discrete source damage) should be considered to assess their residual mechanical properties. Therefore, it is of great importance to develop an efficient prediction model to assess the CAI strength of CFRCs with various LVI damages.

Artificial neural network (ANN) algorithm is a powerful method for modelling a complex nonlinear relationship between inputs and outputs where an accurate analytical expression is difficult to achieve. An elaborate review on the application of ANN to mechanical modelling of composite materials is given by Zhang et al. [26]. Fan and Wang [27] used an ANN-based approach to predict the tensile strength of composite laminates with an open-hole by training the limited number of testing data. Altabay and Noori [28] developed a feed-forward neural networks model to predict the fatigue life of CFRCs as a function of stress ratios, fibre orientations, materials, and loading conditions. Stamopoulos et al. [29] developed two ANNs models which were trained using a multi-scale methodology to predict matrix-dominated mechanical properties (e.g. transverse strength, transverse stiffness, flexural strength, flexural modulus, and short beam strength) of CFRCs with the aid of either the porosity characteristics using X-ray computed topography (CT) or the autoclave pressure, and the predictions were consistent with the mechanical tests. Balokas et al. [30] studied the influence of manufacturing uncertainties of three-dimension(3-D) braided carbon fibre/epoxy composites on elastic modulus and in-plane strength using an ANN-based method. Vineela et al. [31] developed the ANN model to predict the ultimate tensile strength of hybrid carbon/glass short fibre composites and the effectiveness of the method was validated by experiment. Chen et al. [32] developed an integrated numerical approach consisting of direct methods (DM) and ANN algorithm to study how ultimate strength and endurance limit of composite materials.

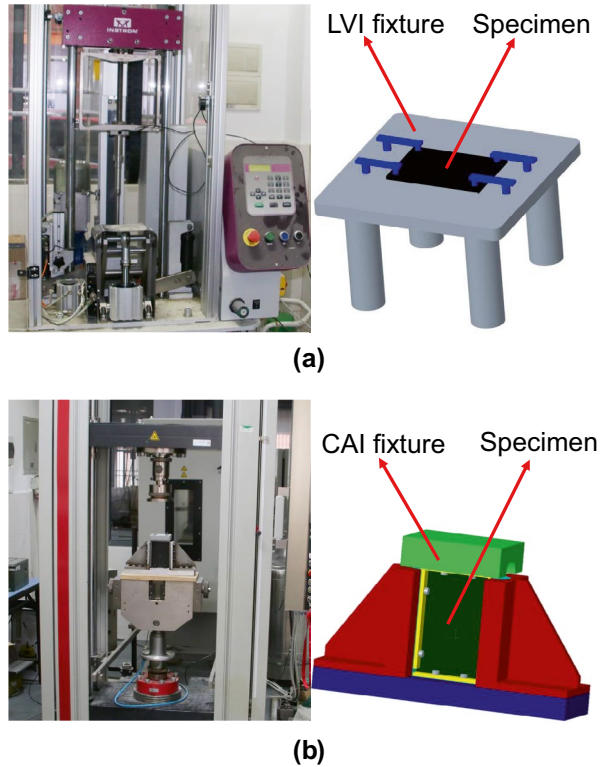
It is well known that the experiments on the CAI strength of CFRC with LVI damage often require a lot of manpower, materials, and financial resources. To meet damage tolerance airworthiness requirements, aircraft composite structures containing various types of damages should be carefully considered to assess their residual mechanical properties. Therefore, it is of great importance to develop an efficient prediction model to assess the CAI strength of CFRCs with various LVI damages. To achieve this goal, this paper aims to develop an efficient ANN-based model together with an FE model to predict the CAI strength of CFRC. First, the FE model considering fibre breakage, matrix cracking and delamination failure was presented to obtain the LVI damage and subsequent CAI behaviour of unidirectional CFRCs. Intra-laminar failure was modelled using Hashin damage criterion [33, 34], while inter-laminar delamination failure was simulated using cohesive interfaces between all plies. Second, the FE predictions were validated with the experimental results. Third, the CAI strengths under various impactor diameters and impact energies were predicted using the present FE model. Then, the nonlinear relationship of the LVI parameters and CAI strength was established with the FE data trained using the ANN method. Finally, the proposed ANN method was validated by the numerical results.

2 Materials and Experimental Setup

2.1 CFRC Preparation

16-ply CFRC laminates (fibre: Toray T300, Japan, epoxy: Techstorm 480, China) were prepared by unidirectional woven fabrics using a vacuum-assisted resin transfer moulding (VARTM) process with a curing temperature of 110 °C at six atmospheres. The stacking sequence of the laminates was $[0^\circ/90^\circ/0^\circ/90^\circ]_2$, and the ply thickness was approximately 0.34 mm. The fibre volume fraction of the cured CFRC laminates was calculated as ~44% based on the areal density of the fabrics and the weight/volume of the laminate. According

Fig. 1 Experiment setup: **a** Instron 9350 drop weight tower, **b** Zwick/Roell machine for CAI test



to the ASTM D7137 standard [35], the CFRC laminates were cut into rectangular specimens with dimensions of $100 \times 150 \times 5.44 \text{ mm}^3$.

2.2 Experimental Setup

According to the ASTM 7136 standard [36], LVI tests on the CFRC specimens were performed using a drop-weight tower (Instron CEAST 9350, USA) as depicted in Fig. 1a. Three hemispherical stainless-steel impactors with diameters of 12.7, 16, and 20 mm and three impact energies (i.e. 20, 33, and 40 J) were considered in this work, as listed in Table 1. The supporting fixture for LVI tests had a $125 \times 75 \text{ mm}^2$ cut-out in the centre, and the CFRC specimen was fixed by four rubber clamps prior to the LVI tests as shown in Fig. 1a.

Table 1 Parameters for the low-velocity impact tests

Tests	Impactor diameter (mm)	Impactor mass (kg)	impactor height (mm)	Initial velocity (m/s)	Impact energy (J)
Case 1	12.7	5.392	624.57	3.50	33
Case 2	16.0	5.392	377.21	2.72	20
		5.392	624.57	3.50	33
		5.392	755.74	3.85	40
Case 3	20.0	5.392	755.74	3.50	33

CAI experiments were conducted on the specimens using a universal testing machine (Zwick/Roell, Germany) as seen in Fig. 1b, in accordance with the standard of ASTM 7137 standard [35]. The specimens were clamped by a CAI fixture (see Fig. 1b) and were compressed along the in-plane direction using a direct-current servo motor with a constant displacement rate of 1 mm/min. At the start of the in-plane compression test, a small force (0.45 kN) was applied to the specimen to ensure the full contact between the specimen and loading surface. Then, the in-plane compression tests were carried out with the measurement of both compressive load and displacement. Each test was repeated twice to obtain the average.

3 Composite Damage Model

3.1 Intra-Laminar Damage

3.1.1 Intra-Laminar Damage Initiation

Hashin failure criterion [33] has been regarded as an effective failure criterion for UD CFRC. Damage initiation occurs when the failure index F reaches or is greater than the unity (1). Hashin’s four damage indices can be calculated according to Eqs. (1–4).

For the fibre tension failure ($\hat{\sigma}_{11} \geq 0$):

$$F_f^t = \left(\frac{\hat{\sigma}_{11}}{X^T} \right)^2 + \alpha \left(\frac{\hat{\tau}_{12}}{S^L} \right)^2 \geq 1 \tag{1}$$

For the fibre compression failure ($\hat{\sigma}_{11} \leq 0$):

$$F_f^c = \left(\frac{\hat{\sigma}_{11}}{X^C} \right)^2 \geq 1 \tag{2}$$

For the matrix tension failure ($\hat{\sigma}_{22} \geq 0$):

$$F_m^t = \left(\frac{\hat{\sigma}_{22}}{Y^T} \right)^2 + \left(\frac{\hat{\tau}_{12}}{S^L} \right)^2 \geq 1 \tag{3}$$

For the matrix compression failure ($\hat{\sigma}_{22} \leq 0$)

$$F_m^c = \left(\frac{\hat{\sigma}_{22}}{2S^T} \right)^2 + \left[\left(\frac{Y^C}{2S^T} \right)^2 - 1 \right] \frac{\hat{\sigma}_{22}}{Y^C} + \left(\frac{\hat{\tau}_{12}}{S^L} \right)^2 \geq 1 \tag{4}$$

where X^T and X^C each denote the tensile strength and compressive strength in the fibre direction. Y^T and Y^C represent the tensile and compressive strength in the transverse direction, respectively. S^L and S^T are the shear strength in the longitudinal and transverse directions, respectively. $\hat{\sigma}_{11}$ and $\hat{\sigma}_{22}$ are the effective normal stress tensors in the fibre direction and transverse direction, respectively. $\hat{\tau}_{12}$ is the shear stress tensor and α is the shear failure coefficient.

3.1.2 Intra-Laminar Damage Evolution

Once the damage initiation criterion was met, the damage starts to evolve with material’s degradation. Damage variables are included in the constitutive equation to describe the damage evolution as

$$\sigma = \frac{1}{D} \begin{bmatrix} (1 - d_f)E_1 & (1 - d_f)(1 - d_m)v_{21}E_1 & 0 \\ (1 - d_f)(1 - d_m)v_{12}E_2 & (1 - d_m)E_2 & 0 \\ 0 & 0 & (1 - d_s)GD \end{bmatrix} \epsilon \quad (5)$$

where $D = 1 - (1 - d_f)(1 - d_m)v_{12}v_{21}$. E_1 and E_2 are the elastic modulus of composite in the fibre direction and the transverse directions, respectively. G is the shear modulus. v_{12} and v_{21} are the major and minor Poisson’s ratios. d_f and d_m are the damage variables that describe the current state of fibre damage and matrix damage, respectively. d_s denotes the current state of shear damage. Damage variables (d_f , d_m and d_s) are derived from the fibre and matrix damage parameters (d_{ft} , d_{fc} , d_{mt} , and d_{mc} , corresponding to the four failure modes as follows:

$$d_f = \begin{cases} d_{ft}, & \text{if } \hat{\sigma}_{11} \geq 0 \\ d_{fc}, & \text{if } \hat{\sigma}_{11} < 0 \end{cases} \quad (6)$$

$$d_m = \begin{cases} d_{mt}, & \text{if } \hat{\sigma}_{22} \geq 0 \\ d_{mc}, & \text{if } \hat{\sigma}_{22} < 0 \end{cases} \quad (7)$$

$$d_s = 1 - (1 - d_{ft})(1 - d_{fc})(1 - d_{mt})(1 - d_{mc}) \quad (8)$$

After the damage initiation (i.e., $\delta_{I,eq} \geq \delta_{I,eq}^0$) as shown in Fig. 2a, the damage variable d_I denotes the reduction of stiffness at the failure mode, which is given as

$$d_I = \frac{\delta_{I,eq}^f (\delta_{I,eq} - \delta_{I,eq}^0)}{\delta_{I,eq} (\delta_{I,eq}^f - \delta_{I,eq}^0)} \quad (d_I \in [0,1], I = ft, fc, mt, mc) \quad (9)$$

where $\delta_{I,eq}^0$ and $\delta_{I,eq}^f$ are the equivalent displacement at damage initiation ($d_I = 0$) and final failure ($d_I = 1$) respectively [1], as shown in Fig. 2b.

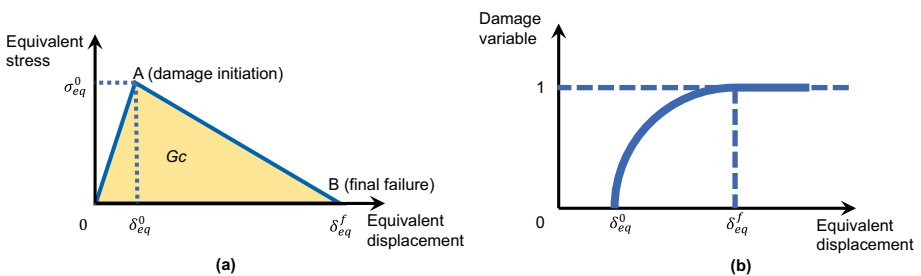


Fig. 2 Damage evolution: **a** equivalent stress versus equivalent displacement relationship, **b** damage variable versus equivalent displacement

The equivalent displacement and stress for the four failure modes depend on the sign of stress and strain components and can be expressed as:

For the fibre tension ($\hat{\sigma}_{11} \geq 0, \epsilon_{11} \geq 0$):

$$\delta_{fi,eq} = L^c \sqrt{\langle \epsilon_{11} \rangle^2 + \alpha \langle \epsilon_{12} \rangle^2} \tag{10}$$

$$\sigma_{fi,eq} = \frac{\langle \sigma_{11} \rangle \langle \epsilon_{11} \rangle + \alpha \tau_{12} \epsilon_{12}}{\delta_{eq}^{fi} / L^c} \tag{11}$$

For the fibre compression ($\hat{\sigma}_{11} < 0, \epsilon_{11} < 0$):

$$\delta_{fc,eq} = L^c \langle -\epsilon_{11} \rangle \tag{12}$$

$$\sigma_{fc,eq} = \frac{\langle -\sigma_{11} \rangle \langle -\epsilon_{11} \rangle}{\delta_{eq}^{fc} / L^c} \tag{13}$$

For the matrix tension ($\hat{\sigma}_{22} \geq 0, \epsilon_{22} \geq 0$):

$$\delta_{mt,eq} = L^c \sqrt{\langle \epsilon_{22} \rangle^2 + \epsilon_{12}^2} \tag{14}$$

$$\sigma_{mt,eq} = \frac{\langle \sigma_{22} \rangle \langle \epsilon_{22} \rangle + \tau_{12} \epsilon_{12}}{\delta_{eq}^{mt} / L^c} \tag{15}$$

For the fibre compression ($\hat{\sigma}_{22} \leq 0, \epsilon_{22} < 0$):

$$\delta_{mc,eq} = L^c \sqrt{\langle -\epsilon_{22} \rangle^2 + \epsilon_{12}^2} \tag{16}$$

$$\sigma_{mc,eq} = \frac{\langle -\sigma_{22} \rangle \langle -\epsilon_{22} \rangle + \tau_{12} \epsilon_{12}}{\delta_{eq}^{mc} / L^c} \tag{17}$$

where L^c is the characteristic length.

3.2 Inter-Laminar Delamination

3.2.1 Delamination Initiation

Delamination occurs when the contact stress ratios reach a value of one based on a quadratic nominal stress function [6]. The delamination initiates when the following equation is met:

$$\left\{ \frac{\langle t_n \rangle}{t_n^0} \right\}^2 + \left\{ \frac{\langle t_s \rangle}{t_s^0} \right\}^2 + \left\{ \frac{\langle t_t \rangle}{t_t^0} \right\}^2 = 1 \tag{18}$$

where t_i ($i = n, s, t$) is the traction stress vector in the normal n and shear directions, s and t , respectively, t_i^0 ($i = n, s, t$) represents the inter-laminar strength under normal stress and two shear stresses, respectively.

3.2.2 Delamination Evolution

Once the delamination initiation criterion is met, the interfacial stiffness starts to degrade as represented using a damage variable d_{inter} . Damage variable $d_{inter} = 0$ indicates no delamination failure, whereas $d_{inter} = 1$ indicates full delamination failure [1]. The damage variable is given by:

$$d_{inter} = \frac{\delta_m^f (\delta_m^{\max} - \delta_m^0)}{\delta_m^{\max} (\delta_m^f - \delta_m^0)} \tag{19}$$

where δ_m^{\max} is the maximum value of the mixed-mode displacement. δ_m^f is the mixed-mode displacement at complete failure, δ_m^0 is the effective displacement when damage is initiated. δ_m is the total mixed-mode displacement (normal, sliding, tearing) written by:

$$\delta_m = \sqrt{\delta_n^2 + \delta_s^2 + \delta_t^2} \tag{20}$$

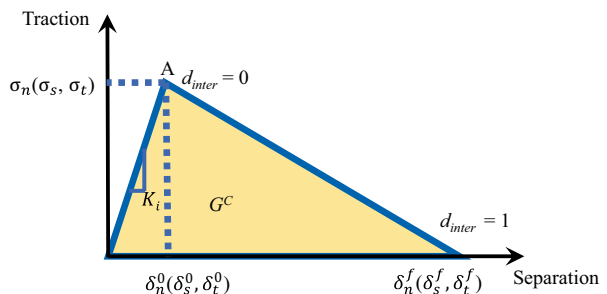
A Benzeggagh-Kenane (BK) fracture energy-based criterion [1] is used to define the mixed-mode displacement for complete failure as:

$$\delta_m^f = \begin{cases} \frac{2}{K\delta^0} [G_{IC} + (G_{IIC} - G_{IC})\xi^\eta] & \delta_n > 0 \\ \sqrt{(\delta_s^f)^2 + (\delta_t^f)^2} & \delta_n \leq 0 \end{cases} \tag{21}$$

where, η is the B–K power law parameter with a value of 1.45, obtained from experiments in literature [37]. $\xi = \frac{\beta^2}{1+\beta^2}$ with ξ taking values between zero and one. When $\xi = 0$ fracture is mode I driven, while as $\xi \rightarrow 1$ is mode II dominated (and this is also the case when $\eta = 0$). β is the mode mixity ratio ($\frac{\delta_n}{\delta_s}$) [1].

When the delamination between each ply is initiated, a degradation of the cohesive properties is calculated based on a bi-linear traction–separation law adopted in the literature [1, 4, 6] (see Fig. 3). The point A represents the material damage initiation. The material deforms in the linear elastic range before the point A and the elastic stiffness is denoted as K_i ($i = n, s, t$). Once the normal or shear traction reaches the ultimate value (point A), delamination occurs and the stiffness

Fig. 3 Traction–separation law of cohesive behaviour used in the finite element (FE) model. G^C represents the fracture toughness



begins to degrade linearly based on the damage evolution variable (Eq. (19)). For the failure under a mixed-mode loading, the damage initiates when the energy release rate $G (=G_I+G_{\text{shear}})$ is greater than the critical energy release rate, with an expressed as:

$$G^C = G_I^C + (G_{II}^C - G_I^C) \left\{ \frac{G_{II} + G_{III}}{G_I^C + G_{II}^C} \right\}^\eta \tag{22}$$

where G_I, G_{II}, G_{III} are the critical fracture energies required to cause failure in the normal, the first, and the second shear directions, respectively. The values of the critical fracture energies are listed in Table 4 which are cited from the literature [4].

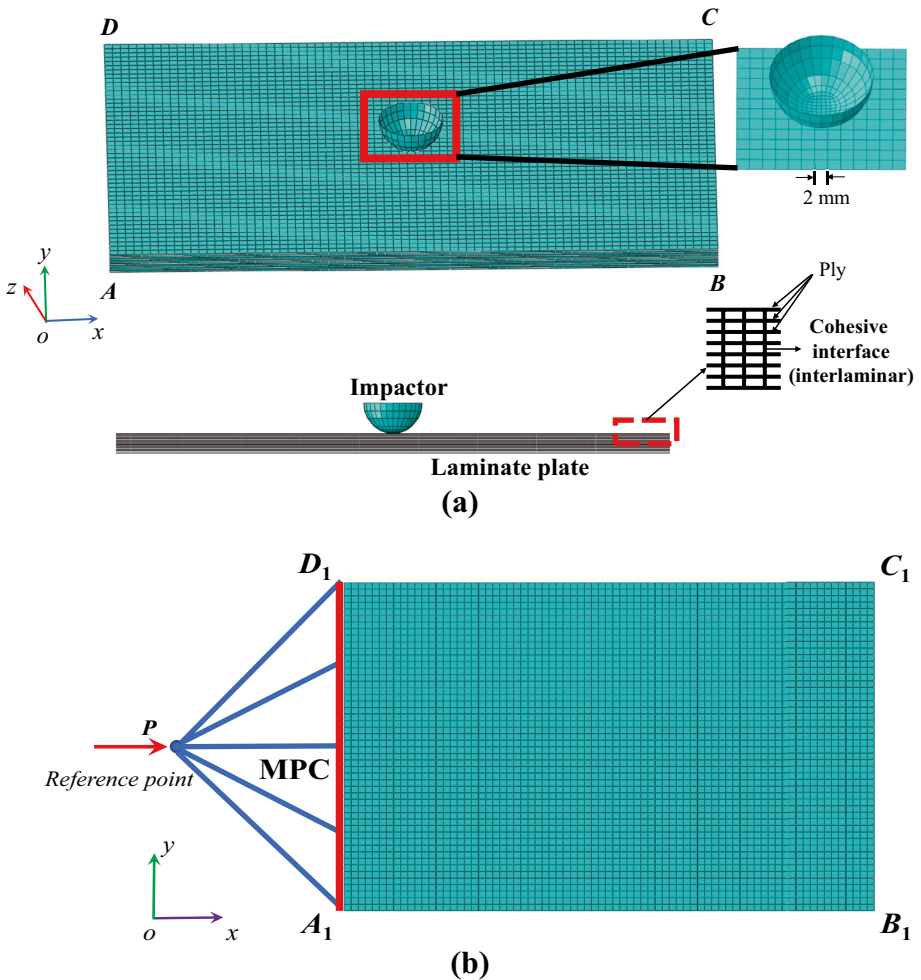


Fig. 4 **a** Schematic of FE model for low-velocity impact analysis. The dimensions of the laminates are $100 \times 150 \times 5.44 \text{ mm}^3$. The four edges of the laminates are fixed, and an initial velocity is assigned to the impactor. **b** Schematic of FE model for compression-after-impact. A displacement condition along the x-direction is applied on a reference point using multi-point constraint (MPC)

Table 2 Boundary conditions of the FE model

Analysis model	Location	Translations			Rotations		
		U_x	U_y	U_z	UR_x	UR_y	UR_z
LVI model	AB, BC, CD and AD	0	0	0	0	0	0
	Impactor	0	0	1	0	0	0
CAI model	A_1B_1	1	1	0	0	0	0
	C_1D_1	1	0	0	0	0	0
	B_1C_1	0	1	0	0	0	0
	Reference point P	1	1	0	0	0	0

*1 represent no restraint, 0 represents restraint

3.3 FE Model

The FE analysis for CFRC with LVI damage subjected to CAI loading was performed using a commercial FE package ABAQUS [25]. Figure 4a shows the LVI FE model and the boundary conditions. The impactor was modelled using a hemispherical rigid body with diameters ranging from 10 to 20 mm. The laminate dimensions were $100 \times 150 \times 5.44$ mm³, consistent with the LVI test coupons. The four edges of the laminates were fixed, and an initial velocity was assigned to the impactor. The initial mesh sensitivity study [6] showed that the mesh size of no more than 2 mm led to negligible differences of the predicted force–displacement curve and damage pattern. Therefore, in this study, the 2×2 mm² four-node doubly curved shell elements were used to mesh the laminate. The total number of elements for the laminate was approximately 60,000, and the total number of nodes was 62,016. The distance between two adjacent layers is equal to the ply thickness. The cohesive contact behaviour which is set between each ply are used to predict inter-laminar damages.

Once the LVI FE analysis was finished, the CFRC laminate with damage were transferred to the CAI FE model as the initial state using “Import Module” in ABAQUS [25]. Meanwhile, the boundary conditions of the FE model were modified for the CAI simulation as shown in Fig. 4b. A quasi-static compressive displacement (1 mm/min) was applied at the reference point attached to the laminate’s left edge using multi-point constraints (MPCs). A “smooth step” was adopted to reduce the dynamic effect. The explicit analysis in ABAQUS was adopted to avoid the severe convergence problem [25]. The damping was neglected in both the LVI and CAI analyses. The detailed boundary conditions used in the LVI and CAI FE models are summarised in Table 2.

3.4 Material Properties and Contact Algorithm

Material properties of the CFRCs are summarised in Table 3 [38, 39]. The fracture toughness for intra-laminar and inter-laminar damage modes were estimated from literature [40, 41]. The cohesive properties of ply interface are given in Table 4 [4]. The contact forces were generated by a penalty contact algorithm. A tangential interaction was defined between contact pairs in terms of a Coulomb friction model. The friction coefficient μ was used to account for the shear stress of the surface traction with contact pressure p , represented as $\tau = \mu p$. The friction coefficient mainly depends on material property and surface

Table 3 Intra-laminar properties of carbon fibre reinforced composites laminate [40, 41]

Items	Values
Density	1445 kg/m ³
Elastic	$E_1 = 153 \text{ GPa}, E_2 = 10.3 \text{ GPa}, G_{12} = 6 \text{ GPa}, \nu_{12} = \nu_{13} = 0.3$
In-plane strength	$X^T = 1637 \text{ MPa}, X^C = 1080 \text{ MPa}, Y^T = 82 \text{ MPa}$ $Y^C = 236 \text{ MPa}, S_{12} = 90 \text{ MPa}, S_{23} = 40 \text{ MPa}$
Intra-laminar fracture energies	$G_{IC}^T = 70 \text{ kJ/m}^2, G_{IC}^C = 50 \text{ kJ/m}^2$
Intra-laminar fracture energies	$G_{IIc}^T = 0.22 \text{ kJ/m}^2, G_{IIc}^C = 1.1 \text{ kJ/m}^2$

quality [42]. Schön [43] measured the friction coefficient for seven surface combinations with fibres in the 0°/0°, 90°/90°, 0°/90°, 45°/0°, 45°/90°, 45°/45° and 45°/-45° directions. The 90° direction was perpendicular to the sliding direction. The specimen pairs with 90°/90° fibre directions had the highest friction coefficient value of 0.5, while the specimen pairs with 0°/0° fibre directions had the lowest friction coefficient value of 0.2. The specimen pairs with 0°/90°, 45°/0°, 45°/90°, 45°/45° and 45°/-45° fibre directions showed friction coefficient values in the range of 0.2–0.5. In the present study, the friction coefficient $\mu = 0.3$ was applied between ply interfaces, which is consistent with the friction coefficient used in literature [42]. Similarly, the friction coefficient between the metal impactor and the composite plate was 0.3.

4 Artificial Neural Network Method

An artificial neural network (ANN) is a group of artificial neurons with a nonlinear mapping capacity inspired by biological central nervous system [44]. It is an adaptive system that can adjust structure according to external or internal information within the network. The three-layer ANN model (Fig. 5) was developed in MATLAB NN Toolbox [45]. The input variables were the impactor diameter and the impact energy of CFRCs. Five neurons were used in the hidden layer to obtain the output of the residual compressive strength.

A sigmoidal activation function with a scaling parameter α and a constant γ , as given in Eq. (22), is adopted to treat the input information (x) in the i^{th} neuron, and then the information is transferred to an output signal (y_i):

$$y_i = \frac{2\alpha}{1 + e^{(-\gamma x_i)}} - \alpha \tag{23}$$

The values of α and γ were taken as 1.0. A linear transfer function was used to provide connections between each layer with an expression as

$$x_j = \sum_{i=1}^m w_{ij} y_i + b_j \tag{24}$$

Table 4 Interfacial properties of carbon fibre reinforced composites laminate [4]

Items	Mode I	Mode II	Mode III
Normalised elastic modulus (GPa)	2.89	2	2
Inter-laminar strength (MPa)	62.3	92.3	92.3
Inter-laminar fracture toughness (kJ/m ²)	0.28	0.79	0.79

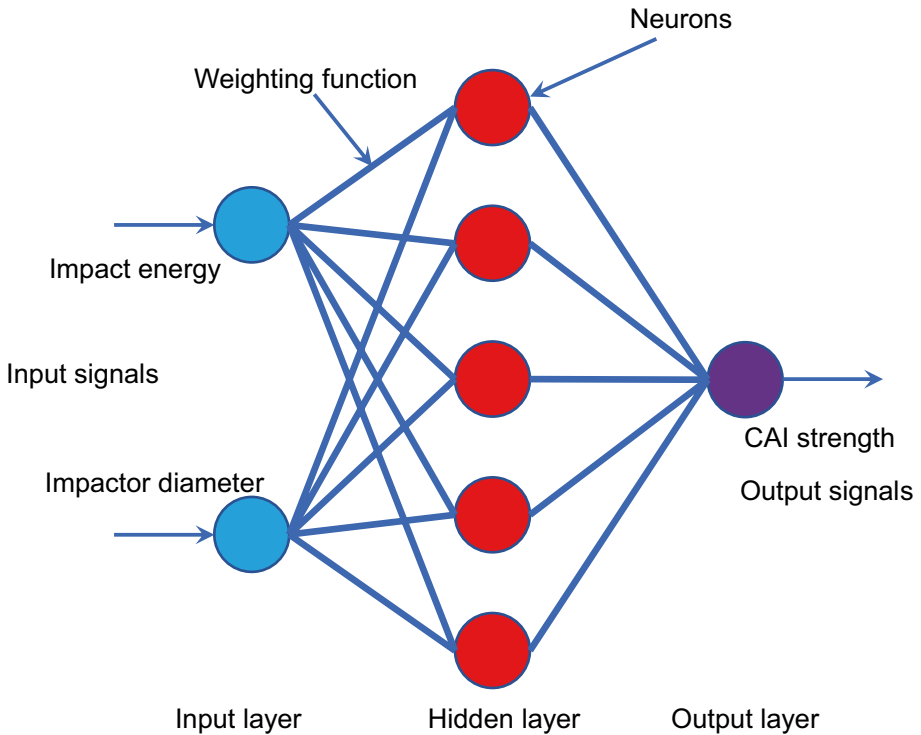


Fig. 5 A three-layer back-propagation (BP) neural network structure, consisting of input, hidden, and output layers

where m is the number of neurons in the layer including i^{th} neuron. w_{ij} is the connection weight. b_j is a constant corrective term [44].

The training data include the input (x) and output (y) parameters. A series of input signals are provided to the neural network of which output signal is already known. The network is trained iteratively to reduce the computed errors (e) between the output signals (y) and the target signals (t). The error is back-propagated through the network to correct the connection weights until the error meet the requirement of the network. Then, the relationship between the input and output signals is obtained to predict the output signals under known input signals. This training method is called back-propagation (BP) learning algorithm [44, 46] and a representative three-layer BP neural network structure is shown in Fig. 4 [47].

When the input signal (x_i) for the i^{th} input neuron propagates through the network to produce output signals (y_j), the computed error (e_j) between the output signal (y_j) and target signals (t_j) can be written as:

$$e_j = t_j - y_j \quad (25)$$

Then, the mean squared error (MSE) for the neural network is calculated.

$$MSE = \frac{1}{n} \sum_{j=1}^n e_j^2 \quad (26)$$

The corresponding root mean square error (RMSE) is as follow:

$$RMSE = \sqrt{\frac{1}{n} \sum_{j=1}^n e_j^2} \tag{27}$$

The connection weights (w_{ij}) are adjusted to minimize a *RMSE* value by comparing the predefined error (Eq. 25) with the computed RMSE (Eq. 27). The incremental form of a connection weight (Δw_{ij}) is expressed as:

$$\Delta w_{ij} = k \frac{\partial E}{\partial w_{ij}} = k \frac{\partial E}{\partial e_j} \frac{\partial e_j}{\partial y_j} \frac{\partial y_j}{\partial x_j} \frac{\partial x_j}{\partial w_{ij}} \tag{28}$$

k is the learning rate parameter. Then, the new connection weight w_{ij}^{new} is updated [48] as follows:

$$w_{ij}^{new} = w_{ij}^{old} + \Delta w_{ij} \tag{29}$$

5 FE Model Validation

5.1 Validation of FE Model for LVI

Figure 6a, e show typical impact force–time histories of the CFRCs under 33 J and 40 J predicted by the experiments and the FE models, respectively. The impact force histories determined by the present FE model are generally consistent with the experimental results. The variations in the impact response curves between FE results and experimental data may be attributed to the ignorance of the damping in CFRC laminate. Although there are

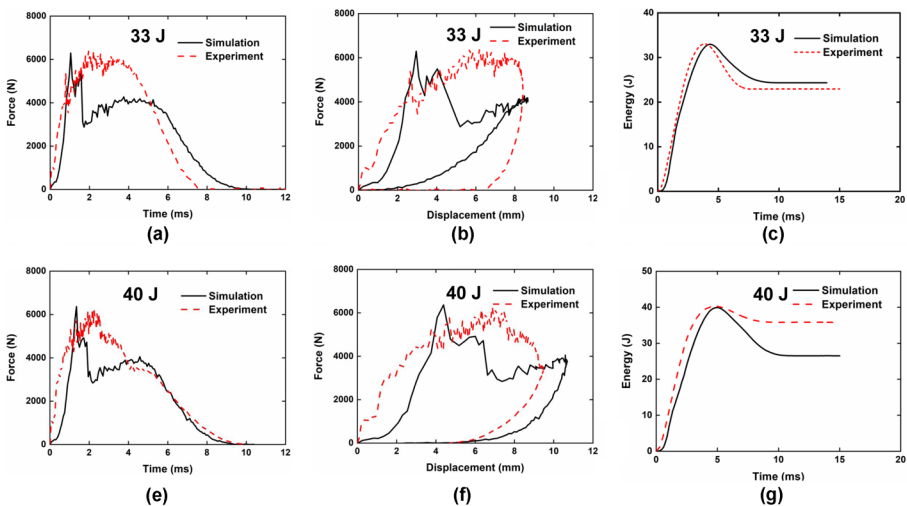


Fig. 6 Impact responses by experiment and simulation under different impact energy, **a** and **e** impact force–time history curves, **b** and **f** impact force–displacement curves, and **c** and **g** absorbed energy history curves

differences between the impact force–displacement curves by FE model and experiment, the predictions in terms of peak impact load, energy absorption curve and failure pattern were in good agreement with the experimental results. Correspondingly, the failure pattern and the ultimate compressive force predicted by the FE model were mostly consistent with the experimental results (Figs. 7 and 11). The impact force increased rapidly in the beginning, and then reached its maximum value followed by a large oscillation due to the damage evolution after ~ 1 ms. Under 33 J impact, the measured maximum impact force was 6295.8 N. This peak impact force is consistent with the predicted maximum impact force of 6410.9 N. The relative percent difference of the measured and predicted peak impact forces was 1.8%. When subjected to a higher impact energy (40 J), the relative percent difference between the predicted and measured maximum impact force was only 1.6%. As shown in Fig. 4b, f, the impact force–displacement relations obtained by the FE model agreed well with the experimental results when subjected to an impact energy of 40 J, whereas the residual deformation obtained from the FE model was smaller than that by the experiment under 33 J impact. In addition, the absorbed energy histories predicted by the FE model and measured by the experiment were similar to each other at the same impact energies, as shown in Fig. 6c, g. Particularly, the predicted absorbed energy under 40 J impact was lower than the experimental result, possibly due to the ignorance of the damping effect in the FE model. Typical visual inspection of the front and back faces of the CFRCs under 33 J impact and the corresponding predicted deformation distributions are compared in Fig. 7. The large deformation and damage were seen in the centre, which is consistent with the observation of the tested specimens. Good agreements between the predicted and measured LVI responses (i.e., impact force–time history, impact force–displacement profile, absorbed energy curve, and damage patterns) demonstrate the effectiveness of the present LVI FE model.

Three primary failure modes resulting from LVI include fibre breakage, matrix cracking and delamination. The distribution of displacement at cross-sectional view of the CFRC laminate after 33 J impact are displayed in Fig. 8. In the figure, the failed elements were removed from the FE model. A good agreement of delamination shapes between experimental and numerical results is found, and the fibre breakage and matrix cracking occur at each ply, which can't be seen in the experimental results. The scanning electron microscope (SEM) images (Fig. 9) clearly show fibre breakage, matrix cracking, and delamination that are consistent with the FE prediction (Fig. 8b). During the impact, matrix cracking occurs first in the impact zone due to its relatively low strength. Shear stresses created between the fibres and the matrices with the impact loading, which eventually result in matrix cracking and delamination failure. With further increase the stress, fibre breakage occurs.

The damage initiation and evolution in the CFRC is obtained during the impact. The typical predicted intralaminar and interlaminar damages in the CFRC under 40 J impact are shown in Fig. 10. At the initial stage, it is seen that slight matrix tensile damage appears at both the front (Fig. 10a) and back faces (Fig. 10b) in the laminate without fibre damage (Fig. 10a, b) and delamination (Fig. 10c) when $t=0.6$ ms. At $t=\sim 1$ ms, the growth of matrix tension damage is seen and delamination occurs in the CFRC, while there are still no fibre damages. Subsequently, the area of matrix tension/compression damages continues to increase and propagate. Meanwhile, slight fibre tension/compression damages also appear at the front and back faces ($t=4.4$ ms). Simultaneously, the delamination damage in CFRCs propagates rapidly as seen in Fig. 10c. After that, during the impact progress, a larger number of matrix damages are observed and fibre damages barely changed at that time.

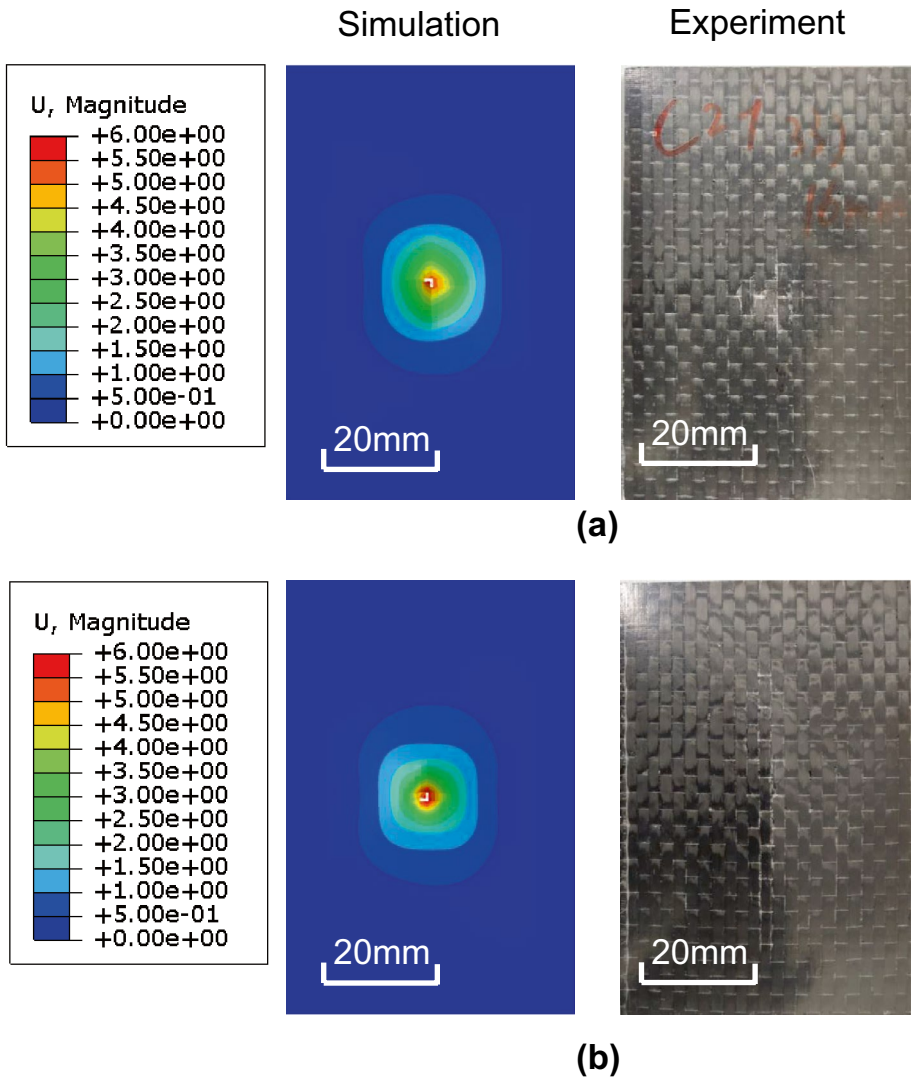


Fig. 7 Experimental and numerical comparison of deformation state after 33 J impact, **a** front face, **b** back face

5.2 Validation of FE Model for CAI Test

Figure 11 shows the damage evolution of the CFRC under the LVI (33 J) and followed by the in-plane compression. In the figure, the red region denotes the fibre compression failure. Fibre compression failure caused by the in-plane compression was the main failure mode for the CAI analysis of CFRCs with initial LVI damages. The fibre compression damage initiated first at the impact zone, and then propagated along the transverse direction, leading to a final local buckling [49, 50]. The ultimate

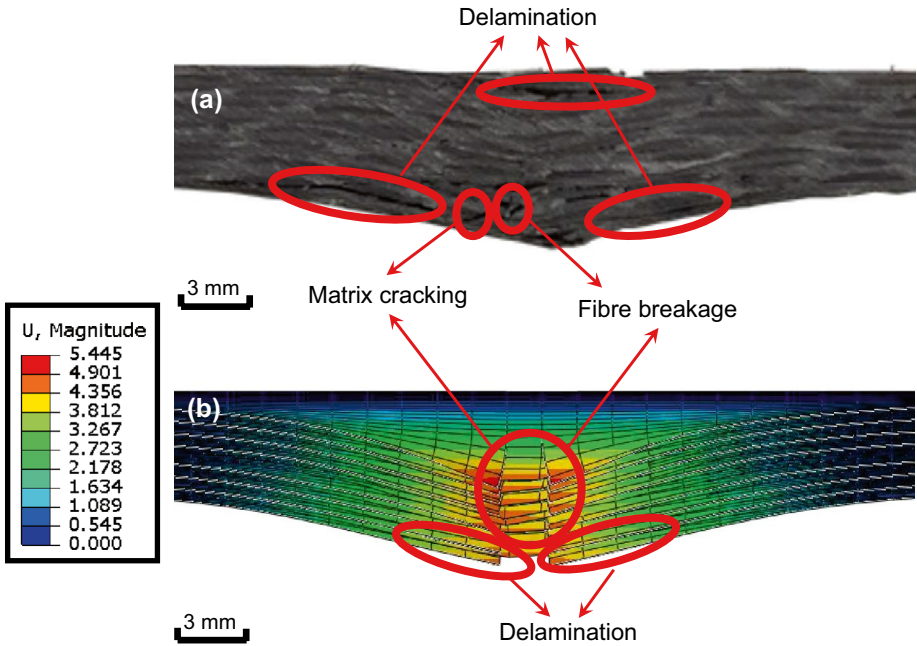


Fig. 8 Cross-sectional observation of failure surface of the specimen by experiment and FE model under 33 J impact

compressive force predicted by the FE model was 67,315 N that was close to that by the experiment (67,280 N) with a 0.09% relative percent difference. The CAI strengths under 33 J impact coincided well with the experimental results. Figure 12 shows the SEM images of the CFRC under LVI and followed by CAI including different failure modes, i.e. fibre breakage, matrix cracking, and delamination failure.

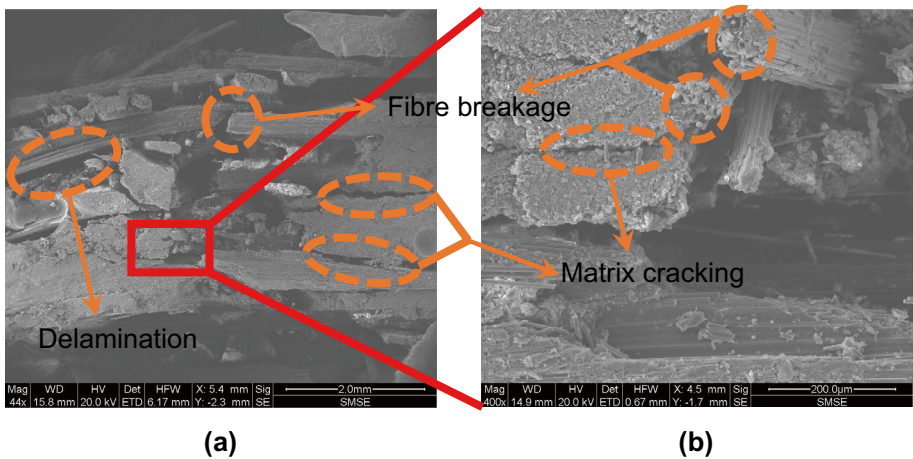


Fig. 9 Scanning electron microscope (SEM) micrographs of carbon fibre reinforced composites subjected to 33 J impact

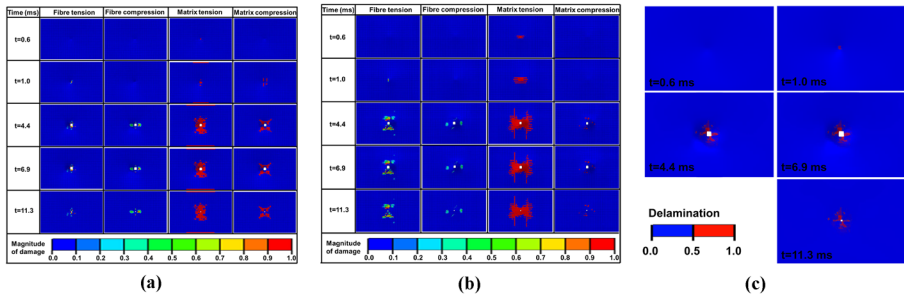


Fig. 10 Damage evolution of the composite laminate under 40 J impact, **a** intralaminar damage at front face, **b** intralaminar damage at back face, **c** projected interlaminar damage area

6 ANN Method for Prediction of CAI Strength

Impactor diameter and impact energy are the two important parameters that determine the CAI strength of the CFRC with LVI damage [51, 52]. In this work, the nonlinear relationship between the impactor diameter, impact energy and the CAI strength was established by the proposed ANN method. Five impactor diameters ranging from 12 to 20 mm were selected herein. Figure 13 shows the predicted CAI strength as a function of the impactor diameter of the CFRCs under 10, 33, and 50 J. The predicted CAI strength of the CFRCs somewhat decreased linearly with the impactor diameter

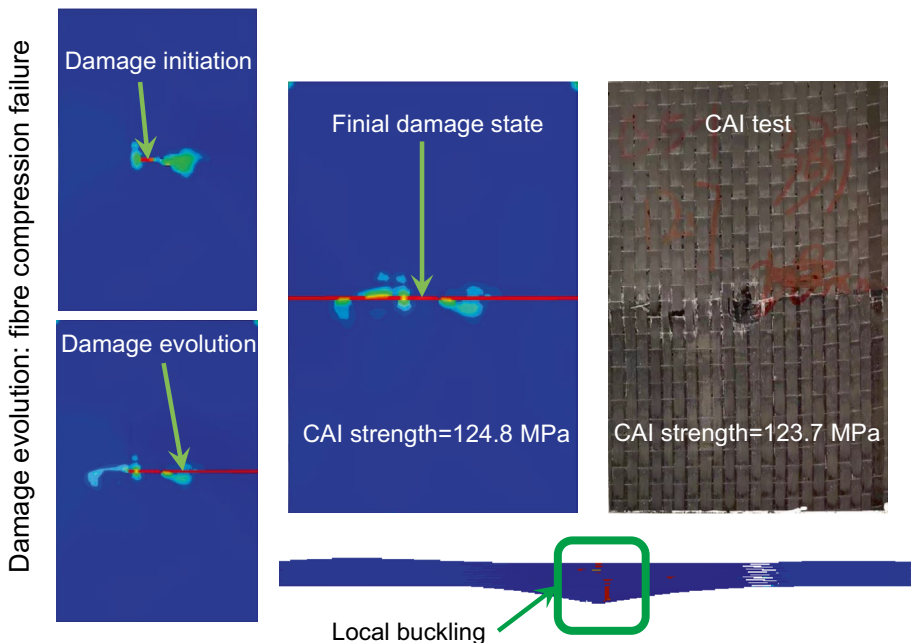


Fig. 11 Damage evolution and failure pattern comparison of the specimen under 33 J impact

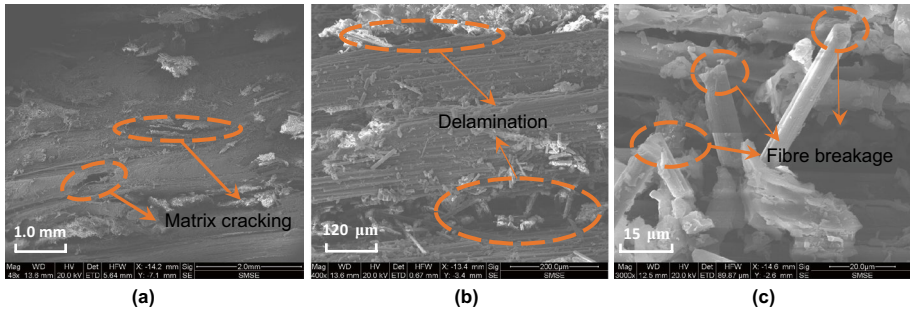


Fig. 12 Scanning electron microscope (SEM) images of the carbon fibre reinforced composites subjected to low-velocity impact (33 J) and followed by in-plane compressive loading

since a larger impactor produces a larger damage/delamination area leading to a lower CAI strength. As expected for the same impactor size, a higher impact energy led to a lower CAI strength.

Various impact energies introduce different LVI damage levels, resulting in different residual compression strength. Figure 14 shows the relationship between the LVI energy and the CAI strength. The residual CAI strength of the CFRCs decreased with the increase in the impact energy. In particular, the CFRC with the 50 J LVI-induced damage showed a nearly 50% reduction in the CAI strength, compared to the undamaged laminated plate (201.0 MPa). As shown in Fig. 14, the influence of the impact energy on the CAI strength is insignificant when the impact energy is larger than 40 J, since the laminate is penetrated by the impactor with an energy of 40 J. Thus, the FE model has obtained some numerical data for the training of ANN to establish the nonlinear relationship between CAI strength and impactor diameter and impact energy.

Table 5 summarises the CAI strengths of the CFRCs with various impactor diameters and impact energies. The other FE model parameters (i.e., geometrical

Fig. 13 Predicted compression after impact (CAI) strength by the FE model versus impactor diameter under three different impact energy (i.e. 10 J, 33 J and 50 J)

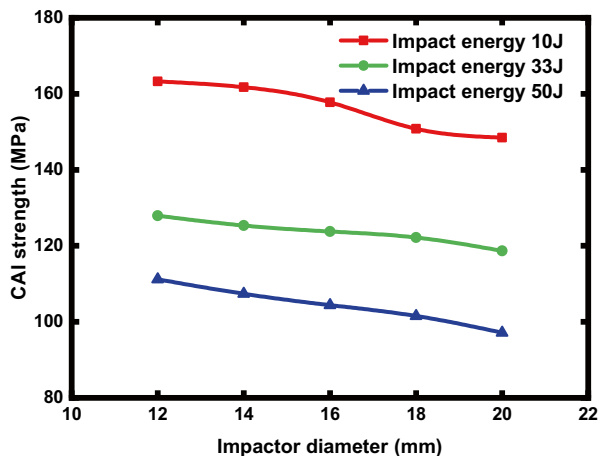
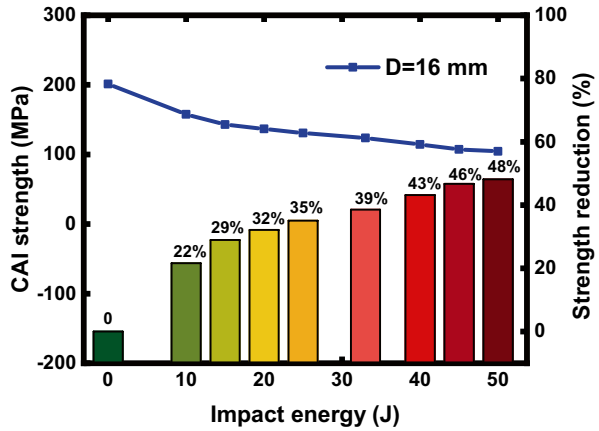


Fig. 14 Compression after impact (CAI) strength by the FE model evaluated at various impact energy values ranging from 0 to 50 J

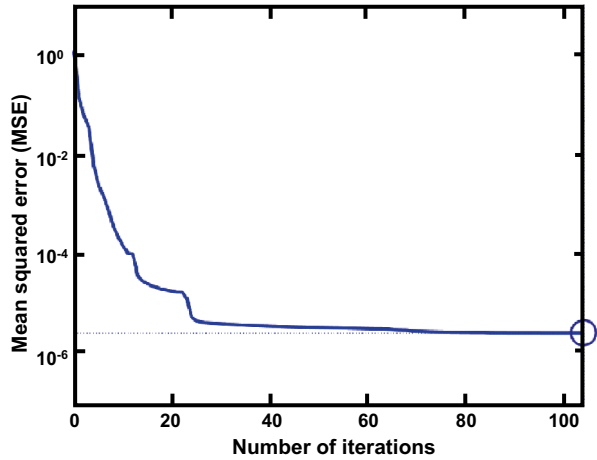


dimension, material properties, stacking sequence) were identical to the test specimen. A total of 20 datasets obtained from the proposed LVI/CAI models were used to perform the data training. Impactor diameter and impact energy were input data and CAI strength was utilised as output data of the ANN model. The MSE of CAI strength (Eq. 25) predicted by the ANN model is depicted in Fig. 15. The training performance was deemed to be satisfactory after 104 iterations, since the value MSE reaches to a

Table 5 Compression after impact (CAI) strength of composite laminates with different impact levels obtained from FE method

Model number	Impact energy (J)	Impactor diameter (mm)	CAI strength (MPa)
No. 1	10	16	157.75
No. 2	15	16	142.96
No. 3	20	16	136.66
No. 4	25	16	130.77
No. 5	33	16	123.74
No. 6	40	16	119.05
No. 7	45	16	107.32
No. 8	50	16	104.39
No. 9	10	12	163.26
No. 10	10	14	161.75
No. 11	10	18	150.83
No. 12	10	20	148.48
No. 13	33	12	127.93
No. 14	33	14	125.32
No. 15	33	18	122.19
No. 16	33	20	118.69
No. 17	50	12	111.20
No. 18	50	14	107.36
No. 19	50	18	101.56
No. 20	50	20	97.15

Fig. 15 Evolution of mean squared error (MSE) versus the number of iterations used for the artificial neural network (ANN) model



design goal value of 3×10^{-6} . The performance of the proposed ANN model was evaluated until MSE reached a design goal of 3×10^{-6} . The predicted MSE substantially decreased to 4.8×10^{-6} after 25 iterations, and then gradually reached the design goal at 104 iterations. Figure 16 compares the CAI strengths predicted by the FE model to the trained results based on the ANN model. A correlation coefficient of determination (R^2) between FE- and ANN-predicted data reflects a good fit. Excellent correlation ($R^2 = 1$) between these two results was reached suggesting that the developed ANN model is capable of accurately training the CAI strength of the CFRCs associated with various LVI parameters (impact energy and impactor diameter).

12 additional sets of CAI strength data of CFRCs with different impactor diameter and impact energy obtained by the proposed numerical model were selected to further validate the present ANN method. Table 6 lists the FE- and ANN-predicted CAI strengths associated with initial LVI with various impactor diameters and impact energy. For all cases considered, the maximum relative percent difference was 4.48%

Fig. 16 Relationship between FE predicted compression after impact (CAI) strengths and ANN predicted CAI strengths. Correlation coefficient $R^2 = 1$

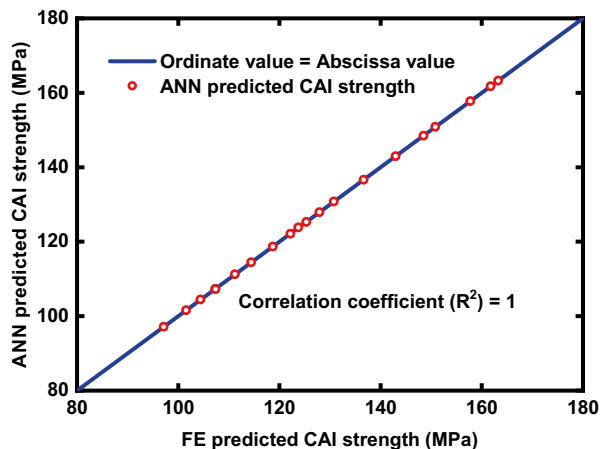
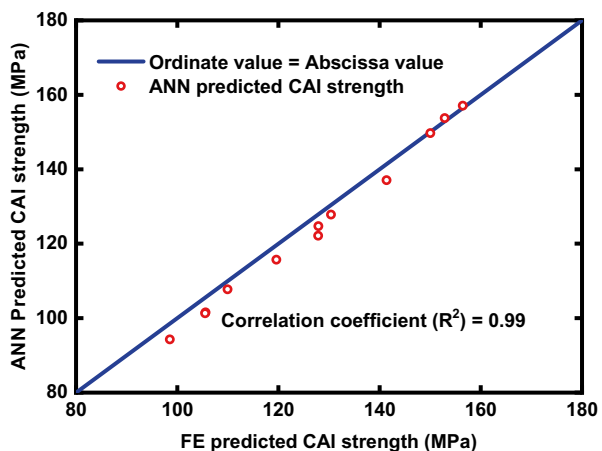


Table 6 Comparison of the FE predicted and artificial neural network predicted (ANN) compression after impact (CAI) strengths

Impact energy (J)	Impactor diameter (mm)	ANN results (MPa)	FE results (MPa)	Relative Percent difference (%)
12	13	156.45	157.08	0.40
12	15	152.87	153.74	0.57
12	17	150.03	149.67	0.24
12	19	141.39	137.04	3.08
30	13	130.39	127.78	2.00
30	15	127.92	124.69	2.53
30	17	127.88	122.15	4.48
30	19	119.62	115.70	3.28
48	13	109.97	107.72	2.04
48	15	105.63	101.56	3.86
48	17	105.54	101.27	4.05
48	19	98.57	94.30	4.33

with an average error value of 2.41% and the coefficient of variation of 0.75%. Figure 17 show a plot of the FE- versus ANN-predicted CAI strengths. A good accuracy ($R^2=0.99$) is achieved with significantly low computation time (~6 s) and costs compared to both FE method and experiment. The ANN-predicted CAI strengths of CFRCs under 30 J and 40 J impact with the impactor diameter=16 mm were 123.68 MPa and 109.13 MPa respectively, while the corresponding experimental values were 123.84 MPa and 114.06 MPa. The maximum error between ANN prediction and experimental results was 4.32% from 40 J impact. Therefore, the proposed ANN model can be used to predict the residual CAI strength of CFRCs with initial LVI damage.

Fig. 17 Relationship between FE predicted compression after impact (CAI) strengths and ANN predicted CAI strengths. Correlation coefficient $R^2=0.99$



7 Conclusions

In this paper, LVI damages including intralaminar and interlaminar cracking in CFRCs are simulated by Hashin damage criterion, quadratic traction criterion for damage initiation, and BK fracture energy-based criterion are adopted for damage evolution. The cohesive contact behaviour is inserted between plies to predict inter-laminar damages. Then, an ANN model was developed to predict the CAI strength of CFRCs, together with the establishment of an FE model considering intra-laminar, and inter-laminar damage. The conclusions are summarised as follows:

1. Two cases of FE models were established according to the corresponding experiments, and the predicted LVI force–time history, force–displacement profile, absorbed energy curves were generally consistent with the corresponding experimental values. The results demonstrated that the proposed FE model can predict the LVI damages of composite structures well.
2. The FE results in terms of residual strength under CAI loading coincided well with the experimental results, and the FE-predicted damage patterns agreed well with the SEM observations in the test specimen, demonstrating the effectiveness of the present CAI FE models.
3. The residual CAI strength decreased with increasing the impact diameter and impact energy. The CAI strength was significantly reduced in the CFRCs after a LVI, even under an impact of 10 J.
4. An ANN model was developed using back-propagation learning algorithm and was trained using the FE results to establish a nonlinear relationship between LVI parameters (i.e. impact energy and impactor diameter) and CFRC residual strength. The ANN-predicted CAI strengths coincided well with the FE predicted CAI strengths. The R^2 value between the two predicted CAI strengths was 0.99, indicating the proposed ANN model is both effective and accurate in predicting the CAI strength of a CFRC for many LVI parameter combinations.
5. It is recommended that more tests offering a more abundant sample sets (e.g., input data: impact energy, impactor diameter, ply thickness, ply sequence and material properties; output data: damage area and CAI strength) contribute to train a more comprehensive and effective prediction model of LVI damage area and CAI strength by ANN technology.

Appendix

In this study, a minimum of two LVI/CAI tests were repeated for each impact energy to ensure the reliability of test data. Figure 18 compares CAI test reproducibility of the CFRCs subjected to initial 33 J LVI. It is clear in the Fig. 18 that two CFRCs showed similar impact damage pattern, compressive load–displacement responses, and peak compressive loads at failure.

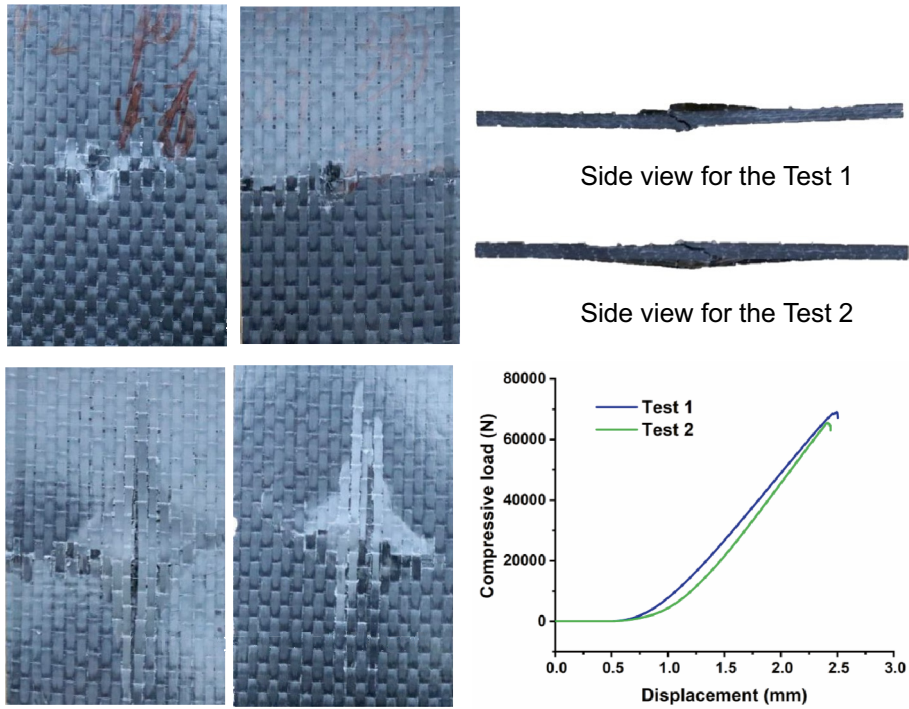


Fig. 18 CAI test reproducibility of the CFRCs under 33 J impact

Acknowledgements The authors are grateful for the support from the Shanghai Pujiang Program (grant number: 19PJ1410000), the National Science Fund for Distinguished Young Scholars (grant number: 11625210), the Fund of State Key Laboratory for Strength and Vibration of Mechanical Structures (grant number: SV2019-KF-04), the Fund of National Postdoctoral Program for Innovative Talents (BX20200244), and the fellowship of China Postdoctoral Science Foundation (2020M671224).

Data Availability The data that support the findings of this study are available from the corresponding author upon reasonable request.

References

- Shi, Y., Swait, T., Soutis, C.: Modelling damage evolution in composite laminates subjected to low velocity impact. *Compos. Struct.* **94**(9), 2902–2913 (2012)
- Prentzas, V., Tsamasphyros, G.: Simulation of low velocity impact on CFRP aerospace structures: simplified approaches, numerical and experimental results. *Appl. Compos. Mater.* **26**(3), 835–856 (2019)
- Wu, Z.Y., Ying, Z.P., Hu, X.D., et al.: Low-velocity impact performance of hybrid 3D carbon/glass woven orthogonal composite: Experiment and simulation. *Compos. B Eng.* **196**, 108098 (2020)
- Qiu, A., Fu, K., Lin, W., et al.: Modelling low-speed drop-weight impact on composite laminates. *Mater. Des.* **60**, 520–531 (2014)
- Davies, G.A.O., Olsson, R.: Impact on composite structures. *Aeronaut. J.* **108**(1089), 541–563 (2004)
- Chen, Y., Hou, S., Fu, K., et al.: Low-velocity impact response of composite sandwich structures: modelling and experiment. *Compos. Struct.* **168**, 322–334 (2017)

7. Schwab, M., Todt, M., Wolfahrt, M., et al.: Failure mechanism based modelling of impact on fabric reinforced composite laminates based on shell elements. *Compos. Sci. Technol.* **128**, 131–137 (2016)
8. Thorsson, S.I., Waas, A.M., Rassaian, M., et al.: Low-velocity impact predictions of composite laminates using a continuum shell based modeling approach part A: Impact study. *Int. J. Solids Struct.* **185**, 185–200 (2018)
9. Cheng, Z., Xiong, J.: Progressive damage behaviors of woven composite laminates subjected to LVI, TAI and CAI. *Chinese J. Aeronaut.* **33**(10), 2807–2823 (2020)
10. Patel, S., Vusa, V.R., Soares, C.G., et al.: Crashworthiness analysis of polymer composites under axial and oblique impact loading. *Int. J. Mech. Sci.* **156**, 221–234 (2019)
11. Lou, X., Cai, H., Yu, P., et al.: Failure analysis of composite laminate under low-velocity impact based on micromechanics of failure. *Compos. Struct.* **163**, 238–247 (2017)
12. Sun, X.C., Hallett, S.R.: Failure mechanisms and damage evolution of laminated composites under compression after impact (CAI): Experimental and numerical study. *Compos. A Appl. Sci. Manuf.* **104**, 41–59 (2018)
13. Debski, H., Rozylo, P., Gliszczynski, A.: Effect of low-velocity impact damage location on the stability and post-critical state of composite columns under compression. *Compos. Struct.* **184**, 883–893 (2018)
14. Sun, W., Guan, Z., Ouyang, T., et al.: Effect of stiffener damage caused by low velocity impact on compressive buckling and failure modes of T-stiffened composite panels. *Compos. Struct.* **184**, 198–210 (2018)
15. Liu, H.B., Liu, J., Dear, J.P., et al.: Effects of impactor geometry on the low-velocity impact behaviour of fibre-reinforced composites: an experimental and theoretical investigation. *Appl. Compos. Mater.* **27**, 533–553 (2020)
16. Liu, D., Bai, R., Lei, Z., et al.: Experimental and numerical study on compression-after-impact behavior of composite panels with foam-filled hat-stiffener. *Ocean Eng.* **198**(15), 106991 (2020)
17. Aryal, B., Morozov, E.V., Shankar, K., et al.: Effects of ballistic impact damage on mechanical behaviour of composite honeycomb sandwich panels. *J. Sandw. Struct. Mater.* (2020)
18. Moumen, A.E., Tarfaoui, M., Hassoon, O.H., et al.: Experimental study and numerical modelling of low velocity impact on laminated composite reinforced with thin film made of carbon nanotubes. *Appl. Compos. Mater.* **25**(2), 309–320 (2018)
19. Liu, H., Falzon, B.G., Tan, W.: Predicting the Compression-After-Impact (CAI) strength of damage-tolerant hybrid unidirectional/woven carbon-fibre reinforced composite laminates. *Compos. A Appl. Sci. Manuf.* **105**, 189–202 (2018)
20. Liu, H., Falzon, B.G., Tan, W.: Experimental and numerical studies on the impact response of damage-tolerant hybrid unidirectional/woven carbon-fibre reinforced composite laminates. *Compos. B Eng.* **136**, 101–118 (2018)
21. Caminero, M.A., García-Moreno, I., Rodríguez, G.P.: Experimental study of the influence of thickness and ply-stacking sequence on the compression after impact strength of carbon fibre reinforced epoxy laminates. *Polym. Testing* **66**, 360–370 (2018)
22. González, E.V., Maimí, P., Camanho, P.P., et al.: Simulation of drop-weight impact and compression after impact tests on composite laminates. *Compos. Struct.* **94**(11), 3364–3378 (2012)
23. Rivallant, S., Bouvet, C., Hongkarnjanakul, N.: Failure analysis of CFRP laminates subjected to compression after impact: FE simulation using discrete interface elements. *Compos. A Appl. Sci. Manuf.* **55**, 83–93 (2013)
24. Habibi, M., Laperriere, L., Hassanabadi, H.M., et al.: Influence of low-velocity impact on residual tensile properties of nonwoven flax/epoxy composite. *Compos. Struct.* **186**, 175–182 (2018)
25. Tuo, H., Lu, Z., Ma, X., et al.: An experimental and numerical investigation on low-velocity impact damage and compression-after-impact behavior of composite laminates. *Compos. B Eng.* **167**, 329–341 (2019)
26. Zhang, Z., Friedrich, K.: Artificial neural networks applied to polymer composites: A review. *Compos. Sci. Technol.* **63**(14), 2029–2044 (2003)
27. Fan, H., Wang, H.: Predicting the open-hole tensile strength of composite plates based on probabilistic neural network. *Appl. Compos. Mater.* **21**(6), 827–840 (2014)
28. Altabey, W.A., Noori, M.: Fatigue life prediction for carbon fibre/epoxy laminate composites under spectrum loading using two different neural network architectures. *International Journal of Sustainable Materials and Structural Systems* **3**(1), 53–78 (2017)
29. Stamopoulos, A.G., Tserpes, K.I., Dentsoras, A.J.: Quality assessment of porous CFRP specimens using X-ray Computed Tomography data and Artificial Neural Networks. *Compos. Struct.* **192**(10), 327–335 (2018)

30. Balokas, G., Czichon, S., Rolfes, R., et al.: Neural network assisted multiscale analysis for the elastic properties prediction of 3D braided composites under uncertainty. *Compos. Struct.* **183**(1), 550–562 (2018)
31. Vineela, M.G., Dave, A., Chaganti, P.K., et al.: Artificial neural network based prediction of tensile strength of hybrid composites. *Materials Today: Proceedings* **5**(9), 19908–19915 (2018)
32. Chen, G., Wang, H., Bezold, A., et al.: Strengths prediction of particulate reinforced metal matrix composites (PRMMCs) using direct method and artificial neural network. *Compos. Struct.* **223**(17), 110951 (2019)
33. Hashin, Z.: Failure criteria for unidirectional fiber composites. *J. Appl. Mech.* **47**(2), 329–334 (1980)
34. Hashin, Z., Rotem, A.: A fatigue failure criterion for fiber reinforced materials. *J. Compos. Mater.* **7**(4), 448–464 (1973)
35. ASTM D7137/D7137M - 12 standard test method for compressive residual strength properties of damaged polymer matrix composite.
36. ASTM D7136/D7136M-15 standard test method for measuring the damage resistance of a fiber-reinforced polymer matrix composite to a drop-weight impact event.
37. Camanho, P.P., Dávila, C.G.: Mixed-mode decohesion finite elements for the simulation of delamination in composite materials. NASA/TM, No. 211737 (2002)
38. Faggiani, A., Falzon, B.G.: Predicting low-velocity impact damage on a stiffened composite panel. *Compos. A Appl. Sci. Manuf.* **41**(6), 737–749 (2010)
39. Jumahat, A., Soutis, C., Hodzic, A.: A graphical method predicting the compressive strength of toughened unidirectional composite laminates. *Appl. Compos. Mater.* **18**(1), 65–83 (2011)
40. Shahid, I., Chang, F.K.: An accumulative damage model for tensile and shear failures of laminated composite plates. *J. Compos. Mater.* **29**(7), 926–981 (1995)
41. Pinho, S.T., Robinson, P., Iannucci, L.: Fracture toughness of the tensile and compressive fibre failure modes in laminated composites. *Compos. Sci. Technol.* **66**(13), 2069–2079 (2006)
42. Shi, Y., Soutis, C.: Modelling low velocity impact induced damage in composite laminates. *Mech. Adv. Mater. Mod. Process.* **3**(1), 14 (2017)
43. Schön, J.: Coefficient of friction of composite delamination surfaces. *Wear* **237**(1), 77–89 (2000)
44. Haykin, S.: *Neural Networks: A Comprehensive Foundation*, 2nd edn. Prentice Hall, NJ (1999)
45. Demuth, H., Beale, M.: *Neural network toolbox for the use with Matlab. User's guide, version 4 The MathWorks* (2002)
46. Hertz, J., Krogh, A., Palmer, R.G., et al.: Introduction to the theory of neural computation. *Phys. Today* **44**, 70 (1991)
47. Barzegar, R., Sattarpour, M., Nikudel, M.R., et al.: Comparative evaluation of artificial intelligence models for prediction of uniaxial compressive strength of travertine rocks, case study: Azarshahr area, NW Iran. *Model. Earth Syst. Environ.* **2**(2), 76 (2016)
48. Ochiai, K., Usui S.: Improved kick out learning algorithm with delta-bar-delta-bar rule, IEEE International Conference on Neural Networks. 269–274 (1993)
49. Sun, X.C., Hallett, S.R.: Barely visible impact damage in scaled composite laminates: experiments and numerical simulations. *Int. J. Impact Eng.* **109**, 178–195 (2017)
50. Ouyang, T., Bao, R., Sun, W., et al.: A fast and efficient numerical prediction of compression after impact (CAI) strength of composite laminates and structures. *Thin-Walled Struct.* **148**, 106588 (2020)
51. Pernas-Sánchez, J., Artero-Guerrero, J.A., Varas, D., et al.: Experimental analysis of ice sphere impacts on unidirectional carbon/epoxy laminates. *Int. J. Impact Eng.* **96**, 1–10 (2016)
52. Liu, P.F., Liao, B.B., Jia, L.Y., et al.: Finite element analysis of dynamic progressive failure of carbon fiber composite laminates under low velocity impact. *Compos. Struct.* **149**, 408–422 (2016)